

**Transverse magneto-optical effects in nanoscale disks**R. Alcaraz de la Osa,<sup>\*</sup> J. M. Saiz, and F. Moreno*Grupo de Óptica, Departamento de Física Aplicada, Universidad de Cantabria, Avenida de los Castros s/n, Santander, Spain*

P. Vavassori

*CIC nanoGUNE Consolider, Tolosa Hiribidea 76, E-20018 Donostia–San Sebastián, Spain and**IKERBASQUE, Basque Foundation for Science, E-48011 Bilbao, Spain*

A. Berger

*CIC nanoGUNE Consolider, Tolosa Hiribidea 76, E-20018 Donostia–San Sebastián, Spain*

(Received 22 September 2011; revised manuscript received 6 December 2011; published 22 February 2012)

We have investigated the optical and magneto-optical responses of nanoscale ferromagnetic disks by means of numerical simulations, using an extension of the discrete-dipole approximation. Specifically, we studied the case of 5 nm thick cobalt disks in the diameter range from 200 to 1000 nm, illuminated under normal incidence with a wavelength of  $\lambda = 632.8$  nm. We furthermore assumed the magnetization to lie in the plane of the disk and to be oriented perpendicular to the electric field of the incoming electromagnetic wave, i.e., the transverse magneto-optical Kerr effect configuration. The induced polarization pattern and the near- and far-field optical and magneto-optical responses have been calculated, finding clear nanoscale confinement effects as one reduces the diameter of the disks. However, we also observe that the rather weak magneto-optical response essentially mimics the optical response, and we demonstrate that it can be calculated as a perturbation of the latter with a high degree of accuracy. This strong similarity between the optical and magneto-optical nanoscale confinement effects also results in the fact that the normalized magneto-optically induced far-field light intensity change, which is the quantity measured in experiments, is only weakly affected even in the case of sub-wavelength-sized disks.

DOI: [10.1103/PhysRevB.85.064414](https://doi.org/10.1103/PhysRevB.85.064414)

PACS number(s): 78.20.Ls, 42.50.Ct, 42.25.Fx, 13.40.–f

**I. INTRODUCTION**

Electromagnetic scattering from nanometer-scale particles is currently a topic of great interest, which is being investigated both theoretically and experimentally for the purpose of understanding the underlying physics and investigate novel near- and far-field optical effects.<sup>1–3</sup> Also, the technological challenge of reducing the scale to work with light has opened new and better possibilities of applications in crucial fields such as those related to health,<sup>4–6</sup> optical communications,<sup>7</sup> information storing,<sup>8</sup> and photonics in general.<sup>9–11</sup> Much of this recent drive has been triggered by the availability of nanofabrication facilities that allow for the design and realization of nanoscale materials.<sup>12</sup> Also, the development of nanometer-scale optical probes such as near-field scanning optical microscopy<sup>13</sup> are a crucial development in this respect. The vast majority of recent studies are performed on metal nanostructures and are focused on the effects on the scattered field due to the excitation of resonances from surface or localized plasmons.<sup>14–17</sup> On the other end, the recent interest in magnetoplasmonics, i.e., solid-state materials that combine magnetic and plasmonic functionalities, has brought forward numerous studies of the interplay between plasmon excitations and magnetism in nanosized or nanoscale defined structures.<sup>18–24</sup> However, little attention has been paid to other potentially interesting effects arising from the mutual interplay between magneto-optical activity and light-matter coupling in spatially confined geometries,<sup>25–27</sup> which are independent of resonance excitations. At the same time, the exploration of these effects poses fundamental questions in magneto-optics

of nanoscale materials and requires new impulses toward experimental<sup>28,29</sup> and modeling efforts.<sup>30–32</sup>

To address these fundamental issues of magneto-optical scattering from nanometer-scale magnetic structures, we developed a modeling approach that relies on a recently developed finite-element computational method, which is an extension of the discrete dipole approximation.<sup>32</sup> The method allows for the calculation of the optical and magneto-optical scattering from nonspherical nanostructures. This aspect is particularly relevant as the majority of experiments are carried out using flat, nonspherical nanometer-scale objects.<sup>26,33</sup> In addition, and since the far-field scattering is measured from a collection of many nano-objects, we have extended the calculations to the experimentally relevant case of an ordered array of noninteracting identical nanostructures.

In order to separate optical and magneto-optical effects that are arising from the nanometer-scale confinement, we have also compared our calculations to a reference case that neglects the effects of the lateral confinement on the induced dipole distribution. Hereby, we define a fictitious (dummy) laterally confined structure made of identical dipoles behaving as if they were part of an infinite film, viz., modeled as a single layer of dipoles under the assumption of translational invariance of the induced dipole moment. This reference case, which has the same level of discretization as well as the same local material properties and approximation assumptions, is what we later call our infinite-layer (IL) approach.

We applied these two approaches to predict the optical and magneto-optical responses in the near and far fields for cobalt disks of sizes from 200 to 1000 nm, illuminated

with a wavelength of  $\lambda = 632.8$  nm under normal incidence. The nanostructures are magnetized in the disk plane and the magneto-optical response is calculated for the so-called transverse magneto-optical Kerr effect (T-MOKE) configuration, in which the electric field of the linearly polarized incoming light is parallel to the scattering plane, while the magnetization of the disk is perpendicular to it.

Our results show that although the nanoconfinement effects appear in the near-field optical and magneto-optical responses of all disk diameters, far-field effects show up only for disks that have a diameter smaller than the wavelength of the incoming light *in vacuo*  $\lambda$ . More importantly, we observe that the optical and magneto-optical contributions to the far-field intensity scale in an almost identical fashion, so that the normalized magneto-optical response, which is the experimentally relevant quantity, is only very weakly affected by the confinement even in the case of sub-wavelength-sized disks.

The work is organized as follows: In Sec. II, the theoretical background, on which our numerical method is based, is presented. In Sec. III, the scattering geometry together with the sample magneto-optical properties are shown. Sec. IV is devoted to the presentation and discussion of the main results obtained from our numerical model. Finally, in Sec. V, the main conclusions of this research are summarized.

## II. THEORY

### A. Finite-particle (FP) approach

Our approach for modeling the optical and magneto-optical responses of nanoscale objects utilizes the recently developed E-DDA (extended discrete dipole approximation) methodology.<sup>32</sup> This extension of the discrete dipole approximation (DDA, also known as the coupled dipole method) has been devised to allow for the calculation of scattering objects with general (scalar or tensorial) electric and magnetic properties. The DDA itself, as well as the E-DDA, relies on the same direct-space discretization scheme that is widely used to study the scattering of light by finite objects. Specifically, the assumptions of this methodology are as follows:

(1) The volume of the object is considered as the union of nonoverlapping, simple connected cells  $j$  of volume  $V_j$  ( $j = 1, \dots, N$ ) with the total volume of the object given by  $V = \sum_j V_j$ .

(2) Each cell  $j$  is assumed homogeneous in its material properties and, because of its small size, the electric and magnetic fields are considered as constant throughout the volume  $V_j$ .

There are two criteria for validity of the DDA:<sup>34</sup> (1)  $|n|kd \lesssim 1$  (so that the dipole lattice spacing  $d$  is small compared with the wavelength of a plane wave in the target material, given by the product  $|n|k$ , with  $n$  being the complex refractive index of the material and  $k = \omega/c$ ), and (2)  $d$  must be small enough ( $N$  must be large enough) to describe the target shape with sufficient precision.

In conventional DDA,<sup>34,35</sup> the optical response of each cell is modeled as the excitation of an oscillating electric point dipole  $\mathbf{P}_j$  located in its center.<sup>36</sup> Cells are built up from a simple

cubic lattice. Each induced electric dipole  $\mathbf{P}_j$  is determined by a polarizability tensor  $\bar{\alpha}_j$ , reacting to a local electric field:

$$\mathbf{P}_j = \varepsilon_0 \bar{\alpha}_j \mathbf{E}_j, \quad (1)$$

where  $\mathbf{P}_j$  is the instantaneous (complex) dipole moment,  $\varepsilon_0$  is the vacuum permittivity, and  $\mathbf{E}_j$  is the instantaneous (complex) electric field at position  $j$  due to all sources external to the  $j$ th cell, i.e., due to the incident electric field at that site and the contributions of all the other  $N - 1$  oscillating dipoles:

$$\mathbf{E}_j = \mathbf{E}_j^{\text{inc}} + \sum_{k \neq j} \bar{\mathbf{A}}_{jk} \mathbf{P}_k, \quad (2)$$

where  $\mathbf{E}_j^{\text{inc}} = \mathbf{E}_0 \exp(i\mathbf{k} \cdot \mathbf{r}_{jk})$  is the incident electric field at position  $j$  and  $\bar{\mathbf{A}}_{jk}$  is the transfer function tensor, describing the electric field at  $j$  created by an oscillating electric dipole at  $k$ , given by

$$\bar{\mathbf{A}}_{jk} \mathbf{P}_k = \frac{1}{4\pi \varepsilon_0} \left[ \mathbf{P}_k \frac{e^{ikr_{jk}}}{r_{jk}} \left( k^2 - \frac{1}{r_{jk}^2} + \frac{ik}{r_{jk}} \right) + \mathbf{r}_{jk} (\mathbf{r}_{jk} \cdot \mathbf{P}_k) \frac{e^{ikr_{jk}}}{r_{jk}^3} \left( -k^2 + \frac{3}{r_{jk}^2} - \frac{3ik}{r_{jk}} \right) \right], \quad (3)$$

where  $k = 2\pi/\lambda$ ,  $\mathbf{r}_{jk} = \mathbf{r}_j - \mathbf{r}_k$ , and  $r_{jk} = |\mathbf{r}_{jk}|$ .

Let us assume that the magneto-optical material is magnetized along the  $z$  direction; then the relative dielectric tensor  $\bar{\varepsilon}_r$  is given by<sup>37</sup>

$$\bar{\varepsilon}_r = \begin{pmatrix} \varepsilon_d & -i\varepsilon_d Q & 0 \\ i\varepsilon_d Q & \varepsilon_d & 0 \\ 0 & 0 & \varepsilon_d \end{pmatrix}, \quad (4)$$

where  $Q$  is the magneto-optical Voigt parameter accounting for the coupling between the electric field and the magnetization. The electric polarizability tensor can be related to the relative dielectric tensor through the well-known Clausius-Mossotti relation, exact for electrostatic (zero-frequency limit) polarizable point dipoles located on a cubic lattice (see, e.g., Purcell,<sup>38</sup> pp. 333–338; Jackson;<sup>39</sup> and Kittel<sup>40</sup>):

$$\bar{\alpha}_j^{\text{CM}} = 3V_j (\bar{\varepsilon}_r - \bar{\mathbf{I}}) (\bar{\varepsilon}_r + 2\bar{\mathbf{I}})^{-1}, \quad (5)$$

where  $\bar{\mathbf{I}}$  is the  $3 \times 3$  identity matrix. At finite frequencies, a radiative correction needs to be added to take into account the phase lag between the incident light and the scattered light radiated by the dipole, due to absorption:<sup>31,41</sup>

$$\bar{\alpha}_j = \bar{\alpha}_j^{\text{CM}} \left( \bar{\mathbf{I}} - \frac{ik^3 \bar{\alpha}_j^{\text{CM}}}{6\pi} \right)^{-1}. \quad (6)$$

Under these conditions, it can be shown that the electric polarizability tensor, neglecting second-order terms,  $O(\varepsilon_{\text{off}}^2)$ , has the following form:

$$\bar{\alpha}_j = \begin{pmatrix} \alpha_d & \alpha_{\text{off}} & 0 \\ -\alpha_{\text{off}} & \alpha_d & 0 \\ 0 & 0 & \alpha_d \end{pmatrix}, \quad (7)$$

where  $\alpha_d$  and  $\alpha_{\text{off}}$  are the diagonal and the off-diagonal elements of the electric polarizability tensor, respectively. Direct application of the E-DDA to the actual disk shape

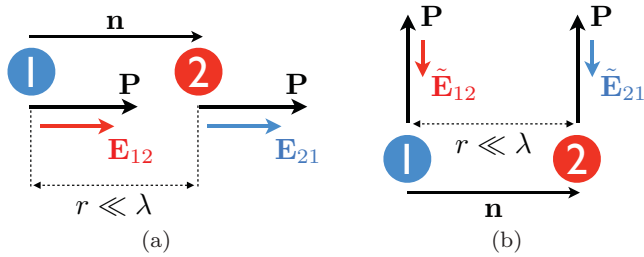


FIG. 1. (Color online) Two interacting electric dipoles in the electrostatic limit. (a) Longitudinal configuration. (b) Transversal configuration.

structure will provide the solution that we refer to as the finite-particle (FP) approach.

Equation (3) gives the electric field produced by an electric dipole at a given distance including near- and far-field contributions. It is instructive for a preliminary discussion to consider only the near-field contribution to the electric field as this provides a good insight into the physics that defines the crucial aspects of this work. The near-field contribution can be obtained from Eq. (3) by imposing that  $r_{jk} \ll \lambda$ . By doing so, we end up with the well-known expression of the electric field produced by an electric dipole  $\mathbf{P}$  at distance  $r$  and direction  $\mathbf{n}$  from the electric dipole, in the electrostatic limit:

$$\mathbf{E}_{\text{nf}} \approx \frac{1}{4\pi\epsilon_0 r^3} [3\mathbf{n}(\mathbf{n} \cdot \mathbf{P}) - \mathbf{P}]. \quad (8)$$

We now consider the particularly simple case of only two interacting electric dipoles. Based on Eq. (8), we can see that two aligned electric dipoles (longitudinal configuration) will produce on each other identical electric fields, as shown in Fig. 1(a). For zero or negligible phase shift, these fields are oriented in the same direction as the induced dipole moment, thus supporting each other:

$$\mathbf{E}_{12} = \mathbf{E}_{21} \approx \frac{1}{4\pi\epsilon_0 r^3} (3\mathbf{P} - \mathbf{P}) = \frac{\mathbf{P}}{2\pi\epsilon_0 r^3}. \quad (9)$$

On the contrary, two parallel electric dipoles (transversal configuration) that are oriented perpendicular to their connecting vector, as shown in Fig. 1(b), will produce identical electric fields that are antiparallel to the direction of the induced dipole moment, thus counteracting each other:

$$\tilde{\mathbf{E}}_{12} = \tilde{\mathbf{E}}_{21} \approx -\frac{\mathbf{P}}{4\pi\epsilon_0 r^3}. \quad (10)$$

Moreover, for a given interacting distance in the near-field range, the longitudinal configuration is more efficient than the transversal one, in the sense that the electric field produced by the electric dipoles in the first case is twice that produced by the transversal configuration, as stated by Eqs. (9) and (10).

We will see later how this simple picture explains key aspects of the relevant physics described by our numerical simulations.

### B. Infinite-layer (IL) approach

For the purpose of evidencing finite lateral size effects in our calculations, we implemented a numerical approach to the problem having the same level of local property representation

and numerical approximations but which neglects the effects of the lateral confinement on the induced dipole distribution. Therefore, we calculated the polarization [Eq. (2)] induced in a laterally infinite film, modeled as a single layer of dipoles [each of them having an electric polarizability  $\tilde{\alpha}_j$  given by Eq. (6)], under the assumption of translational invariance of the induced dipole moment  $\mathbf{P}_{\text{IL}}$ . Subsequently, this induced dipole  $\mathbf{P}_{\text{IL}}$  is inserted in each cell of the discretization mesh to model any arbitrary planar shape (no further interaction is considered). Due to the normal incidence geometry, the translational invariance of this approach does not require phase factors for the electric field of the incoming wave front. Details of this discretized IL reference model are described in the Appendix.

### III. SAMPLE GEOMETRY AND MATERIAL PARAMETERS

In order to obtain the optical and magneto-optical responses of disk-shaped objects, we have used material parameters of cobalt, as given in Ref. 42 with  $\epsilon_r = -12.6 + 22.88i$  and  $Q = 0.034 + 0.014i$ , for  $\lambda = 632.8$  nm. All calculations are performed twice: first as fully self-consistent FP particle calculations, and then for comparison purposes within the framework of the IL approach. Figure 2 shows the specific MOKE configuration used here, with a set of disks arranged on a two-dimensional square lattice of period  $a$ . The scattering properties of the complete lattice will be considered specifically in Sec. IV B 2. The disks are illuminated by a monochromatic incident beam under normal incidence. The incident electric field  $\mathbf{E}_j^{\text{inc}}$  is linearly polarized along the  $y$  direction and the sample magnetization is perpendicular to the

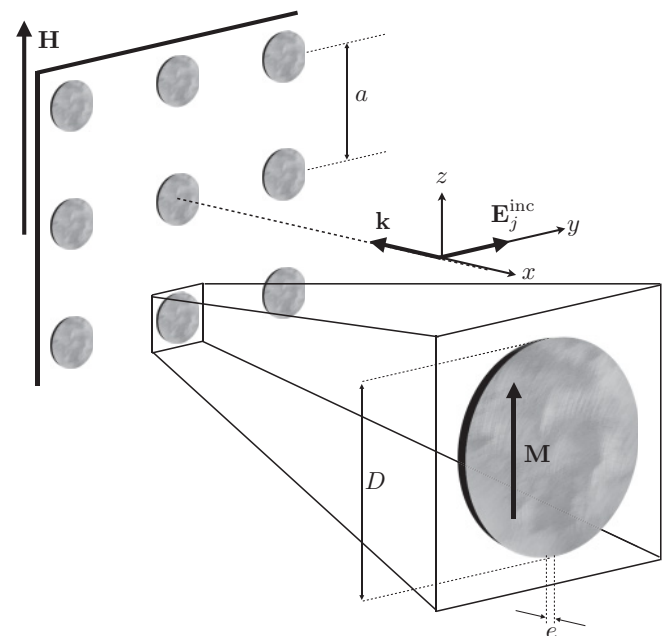


FIG. 2. T-MOKE configuration typically used in an experimental setup, with an array of disks of thickness  $e$  with constant lattice period  $a$  along both surface-plane dimensions. The incoming-light wave vector, with  $\lambda = 632.8$  nm, is in the  $-x$  direction, the incident electric field  $\mathbf{E}_j^{\text{inc}}$  is linearly polarized along the  $y$  direction, and the magnetization  $\mathbf{M}$  is perpendicular to the chosen scattering plane (considering the  $X$ - $Y$  plane).

incident electric field, so that the wave vector  $\mathbf{k}$ , the incident electric field  $\mathbf{E}_j^{\text{inc}}$ , and the magnetization  $\mathbf{M}$  are all orthogonal to each other. This arrangement corresponds to the T-MOKE geometry where changes in the sample magnetization lead to changes in the intensity of the scattered field, leaving its polarization state unchanged.<sup>37</sup> Applying the above values in Eq. (4), the relative dielectric tensor becomes (assuming that the external magnetic field is large enough to reach magnetization saturation along the  $z$  axis of the sample)

$$\bar{\epsilon}_r = \begin{pmatrix} \epsilon_d & \pm\epsilon_{\text{off}} & 0 \\ \mp\epsilon_{\text{off}} & \epsilon_d & 0 \\ 0 & 0 & \epsilon_d \end{pmatrix}, \quad (11)$$

where  $\epsilon_d = -12.6 + 22.88i$  and  $\epsilon_{\text{off}} = 0.60152 + 0.74872i$ . Notice as well that, according to the T-MOKE configuration shown in Fig. 2 (magnetization  $\mathbf{M}$  in the  $z$  direction), only the diagonal and the  $xy$  elements of the dielectric tensor are different from zero, with their sign depending on the direction of the magnetization along the  $z$  axis.

In our numerical calculations, different diameters for the disks have been considered, ranging from  $D = 200$  nm to  $D = 1000$  nm, with all of them having a thickness of  $e = 5$  nm. The lattice period  $a$  has been chosen large enough, ranging from 700 nm to 15  $\mu\text{m}$ , that interactions between the disks are very weak and can be neglected. Thus, we can simplify our simulations to calculations on a single disk only and, with these results, predict the diffracting behavior of the entire array under uniform illumination. The single disk simulations have been performed by using the E-DDA code, with a dipole spacing of  $d = 5$  nm. Correspondingly, we only consider a single layer of electric dipoles for cubic cells of volume  $V_j = d^3$ . We used a grid with  $d = 5$  nm that is much finer than the widely used one<sup>34</sup> based on  $|n|kd \lesssim 1$ , which would correspond to  $d < 20$  nm.<sup>43</sup> Calculations using a finer grid of  $d = 2.5$  nm produced no significant changes in the results.

The E-DDA code solution is based on an iteration scheme that uses the complex-conjugate gradient (CCG) method with enhancement to maintain convergence in finite-precision arithmetic.<sup>44</sup> Being an iterative technique, the CCG requires an initial guess for  $\mathbf{P}_j$ . Here, we assume that the electric dipoles are initially excited by the incident electric field only, so that

$$\mathbf{P}_j^{\text{initial}} = \epsilon_0 \bar{\alpha}_j \mathbf{E}_j^{\text{inc}}. \quad (12)$$

In each iteration, a new solution for the dipole moment,  $\mathbf{P}_j^{\text{new}}$ , is found. The cutoff criterion for self-consistency in all our calculations, if not stated otherwise, is

$$\frac{|\mathbf{P}_j^{\text{new}} - \mathbf{P}_j|}{|\mathbf{P}_j|} \leq \text{TOL}, \quad (13)$$

where TOL is the error tolerance, set to  $\text{TOL} = 10^{-5}$  in order to solve the problem to high accuracy (see Sec. 11 in Ref. 45).

The scattered intensity  $I$  is defined as the absolute value of the time-averaged Poynting vector  $\langle \mathbf{S} \rangle$ , calculated as  $\langle \mathbf{S} \rangle = \frac{1}{2} \text{Re}\{\mathbf{E} \times \mathbf{H}^*\}$ , where  $\mathbf{E}$  and  $\mathbf{H}$  are the scattered electric and magnetic fields, respectively.<sup>46</sup> Of course, the scattered intensity is strongly angle dependent.

In the single-layer calculation, all dipoles are contained in a planar structure, so that in the absence of magneto-optical

effects, only the  $y$  and  $z$  components of the local polarization are different from zero. This allows us to easily relate the out-of-plane ( $x$ ) component of  $\mathbf{P}_j$  with the MO contribution.

It is important to note that the general observations made here would still hold if one were to replace the single-layer calculation with a multilayer calculation, but it is not as straightforward to isolate the magneto-optically induced polarization pattern in this case.

The T-MOKE is usually characterized by the parameter  $\Delta I$ , which here we define as the absolute change in the intensity of the light scattered by a medium when the magnetization  $\mathbf{M}$  of the medium is reversed:

$$\Delta I = |I(M) - I(-M)|, \quad (14)$$

where  $I$  is the scattered light intensity.

## IV. RESULTS AND DISCUSSION

### A. Dipole moment distributions

A comparison of the resulting polarization pattern is summarized in Fig. 3, where the spatial distributions of the primary optical ( $y$  component) and MO ( $x$  component) dipole moment are shown for a set of disks, ranging from  $D = 200$  nm to  $D = 1000$  nm, calculated with the FP approach and normalized by the dipole moment obtained with the IL reference method; i.e. (on each cell  $j$ ),

$$|P_y| = \frac{|P_y|_{\text{FP}}}{|P_y|_{\text{IL}}} \quad \text{and} \quad |P_x| = \frac{|P_x|_{\text{FP}}}{|P_x|_{\text{IL}}}. \quad (15)$$

The first thing to notice when looking at Fig. 3 is that the distributions of  $|P_y|$  and  $|P_x|$  are not homogeneous and show noticeable departures from 1; i.e., there are important confinement modifications to both the primary optical ( $y$ ) and the MO ( $x$ ) responses of the disks. The second important aspect that is visualized by the polarization pattern in Fig. 3 is the fact that the MO response pattern is very similar to, if not outright indistinguishable from, the lateral  $P_y$  structure, indicating that the magneto-optical effect is a small perturbation of the optical response and thus mimics its behavior. These results are in agreement with recent results obtained by other authors.<sup>47</sup>

In general, a confined geometry results in the appearance of different oscillation modes in the dipole amplitude spatial distribution, coming from the finite-size (and shape) self-interaction. This is clearly seen in the third row of Fig. 3, where line profiles along the  $y$  direction ( $z = 0$ ) are shown for both the primary optical (red lines) and the magneto-optical (blue lines) component. These geometry-induced interactions not only modify the lateral distribution of the dipole pattern but can also result in collective effects, as hinted by the overall enhancement found in the smallest disk size shown,  $D = 200$  nm, Fig. 3(a). Indeed, the  $D = 200$  nm presents the most important deviation from the IL approach, with high values of the dipole moment even in the central region of the disk.

The case  $D = 400$  nm [Fig. 3(b)] already starts to show the appearance of a new central minimum, as well as two regions with high values of dipole moment. This is clearly seen in the case  $D = 600$  nm [see Fig. 3(c)]. As  $D$  increases, Figs. 3(d) and 3(e), the oscillation of the spatial distribution of

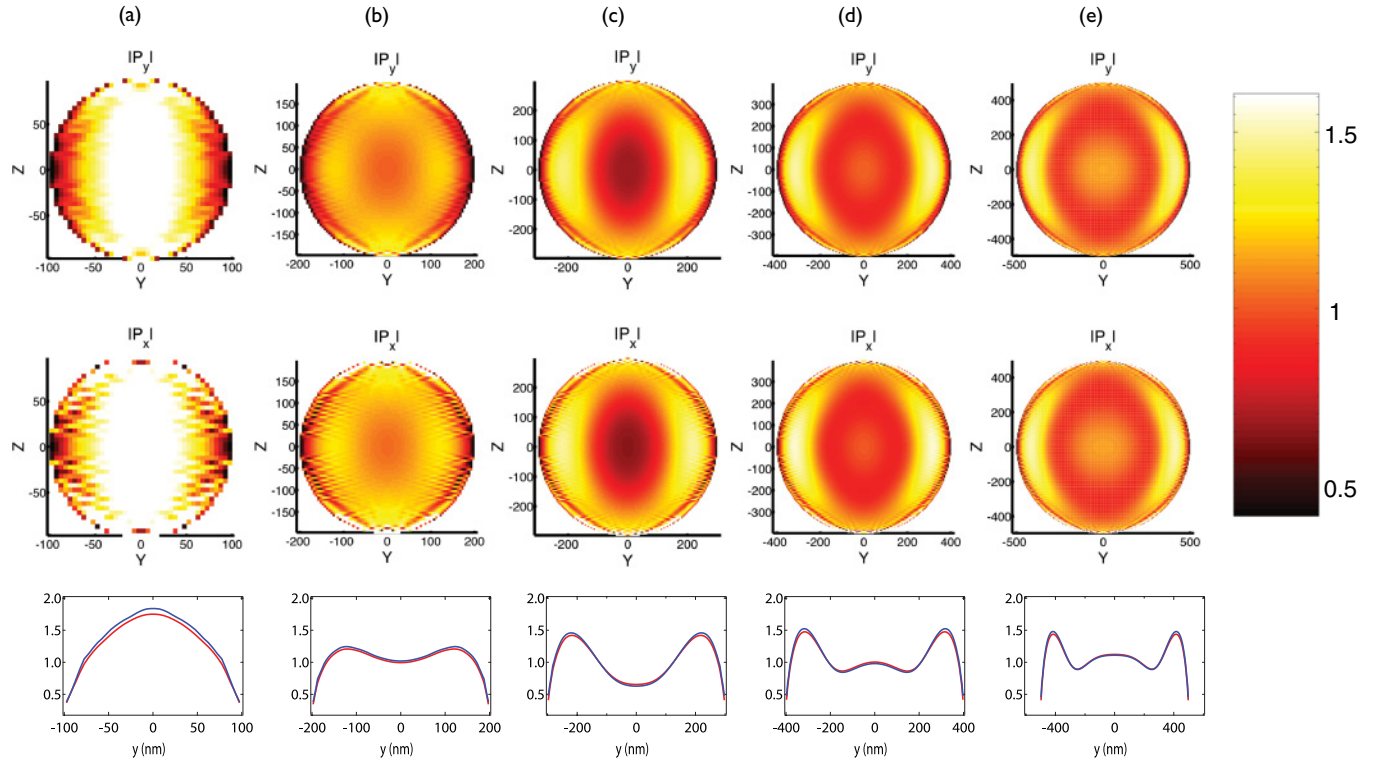


FIG. 3. (Color online) Absolute value of the primary optical ( $y$ ) and MO ( $x$ ) components of the induced dipole moment for several sizes normalized to the IL calculation. From left to right, each column corresponds to one disk size, (a)  $D = 200$  nm, (b)  $D = 400$  nm, (c)  $D = 600$  nm, (d)  $D = 800$  nm, and (e)  $D = 1000$  nm. The color scale is the same for all maps. The third row shows line profiles along the  $y$  direction ( $z = 0$ ) for both the primary optical (red lines) and the magneto-optical (blue lines) components.

the dipole moment amplitude appears, resulting in new minima and maxima that nucleate in the center of the disk and expand (and squash together) toward the edges.

Both in the optical and the MO components, the phase distributions are all very uniform, the dipole moments inside the particle being almost in phase with the IL reference dipole.

Following the simple arguments presented when discussing the case of two interacting electric dipoles, we can understand two important features of the maps of the primary optical response, i.e., the  $y$  component, shown in the first row of Fig. 3. For all sizes, it is found that along the  $y$  direction, there is a decrease near the boundaries of the disk. This can be explained due to the absence of neighboring electric dipoles outside the particle. The missing dipoles would be supporting those at the boundary, the same way neighboring dipoles support each other in the interior of the disk due to their alignment [see Fig. 1(a)]. Thus the induced dipole moment at the boundary is smaller than inside the disk or in the case of the IL reference calculation, for which the neighbors extend to infinity.

In the case of the MO ( $x$ ) response (see Fig 3, second row), it can be seen that it follows the  $P_y$  even in the boundary region.

In order to show the global behavior of the induced dipole moment in the disks as a function of both the MO constant  $Q$  and the size, we have calculated the averaged dipole moment inside the disks. In Fig. 4, all results correspond to the spatial average over the disk, normalized to the IL results:

$$|\langle P_y \rangle| = \frac{|\langle P_y \rangle|_{\text{FP}}}{|P_y|_{\text{IL}}} \quad \text{and} \quad |\langle P_x \rangle| = \frac{|\langle P_x \rangle|_{\text{FP}}}{|P_x|_{\text{IL}}}. \quad (16)$$

Fig. 4 shows the absolute value of the averaged primary optical ( $y$ ) and MO ( $x$ ) components of the induced dipole moment normalized to IL results, as a function of the disk diameter  $D$ .

Obviously, the averaged dipole moment in the FP calculation tends to the IL when the size of the disk is increased, and therefore the average of the relative amounts tends to 1, as observed in Figs. 4(a) and 4(b). As we decrease the disk diameter, the average dipole moment grows, according to what we had already discussed in relation to the case of the  $D = 200$  nm disk and its induced polarization distribution [Fig. 3(a)]. Again, we can see how the MO component enhancement resembles the optical one, although they are not fully identical (one can see quantitatively that the overall  $P_x$  enhancement is a bit larger than the  $P_y$  enhancement for small disks,  $D \leq 400$  nm). These results indicate that we are in the small perturbation regime of magneto-optics. In order to corroborate this, we have performed calculations varying the strength of the magneto-optical coupling  $Q$ , either dividing it or multiplying it by 10, which is also shown in Fig. 4 (blue squares and black triangles, respectively).

It is clearly seen from the results in Fig. 4 that, if we make the MO coupling constant  $Q$  ten times either smaller or larger, the results normalized to a corresponding IL calculation are completely preserved. This confirms that we are in the linear perturbation regime,<sup>47</sup> as anticipated by the close similarity of the  $x$  and  $y$  patterns in Fig. 3. It is important to keep in mind that, of course, the magneto-optical effect is changed with  $Q$ , but this is normalized out by the IL normalization. Thus,  $Q$ ,  $Q/10$ , and  $Q \times 10$  are perfectly linear in the

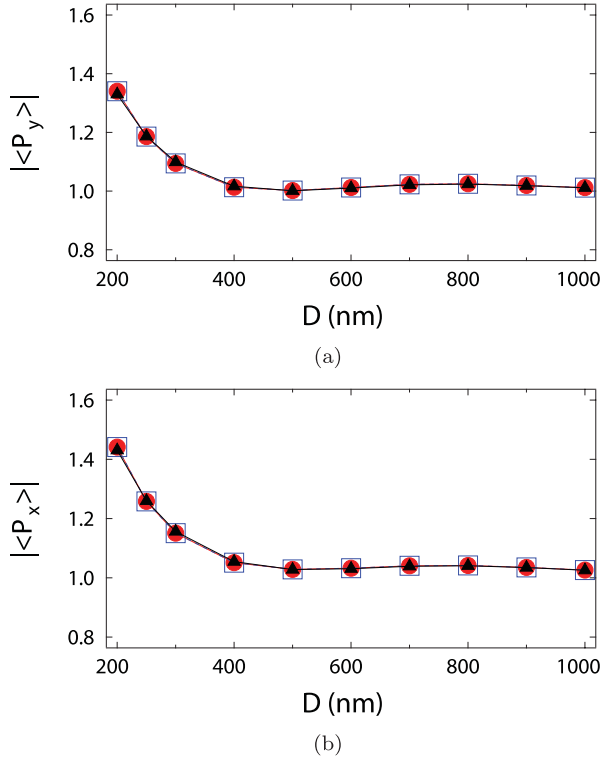


FIG. 4. (Color online) Absolute value of the averaged (a) primary optical ( $y$ ) and (b) MO ( $x$ ) components of the induced dipole moment for three different values of the MO constant (full red circles for  $Q$ , blue squares for  $Q/10$ , and black triangles for  $Q \times 10$ ), as a function of the disk diameter  $D$ .

MO-induced effects. This point will be addressed in further detail in Sec. V.

## B. Far field

Experimental measurements of MO effects rely primarily on far-field observation of the scattering changes induced by the presence of a net magnetization. In this section we first calculate and discuss the properties of single disks to achieve a good understanding of their general response. Then, we derive and discuss the magneto-optical response of an array of disks, since experiments make use of arrays.

### 1. Single disks

Figure 5 shows the far-field patterns of scattered intensity  $I$  and the MO signal  $\Delta I$  calculated in the  $X$ - $Y$  plane, which is the relevant plane for T-MOKE. The IL reference calculation is also shown, in order to compare both approaches and illustrate the confinements effects.

According to the previously discussed findings on the optical and MO dipole distributions, the far-field scattered intensity patterns converge to those obtained with the IL approach (see first row of plots in Fig. 5), as the disk diameter is increased. All disks show mostly dipolar behavior, i.e., a two-lobe scattering pattern with almost no scattered intensity at  $90^\circ$  and  $270^\circ$  (direction of oscillation of the incident electric field). In the case of small disks ( $D < \lambda$ ), a size-dependent

enhancement of the scattering intensity is observed. Moreover, scattering from large disks tends to be more directional, around the forward and backward directions, as should be expected for particles of radius larger than the wavelength. The case  $D = 200$  nm clearly shows the biggest difference between FP and IL in both  $I$  and  $\Delta I$ , in accordance to results shown in Fig. 3, indicating that phase changes inside the particle are minimal.

The  $\Delta I$  patterns (second row in Fig. 5) show values about three orders of magnitude smaller than the scattered intensity  $I$  patterns, this ratio being consistent with the relative magnitude between the MO and optical effects in a material such as Co. As in the case of the  $I$  patterns, the  $\Delta I$  patterns also converge to those obtained with the IL reference method upon increasing the disk diameter. In the forward and backward directions (transmission and reflection, respectively),  $\Delta I$  is zero, since at those directions, the MO response produces *only* a second-order scattering effect [see Eq. (3) in Ref. 48], which is insensitive to the sign of  $\mathbf{M}$  and thus does not show up in a difference measurement based upon magnetization reversal, such as  $\Delta I$ . Along the  $90^\circ$  and  $270^\circ$  direction, the scattered intensity coming from dipoles oscillating along the  $x$  direction is maximum, although insensitive too to the direction of magnetization, therefore producing a deep minimum of  $\Delta I$  along this axis. The characteristic four-lobe shape of these patterns arises as a consequence of those minima. Of course the curve shape and the direction of the maxima depend on both the relative phase of the radiation coming from the optical and magneto-optical dipoles as well as on the different optical paths, so that they cause an intensity change that depends strongly on the radiation direction.

The normalized MO signal,  $\Delta I/I$ , the so-called figure of merit of T-MOKE, remains nearly constant, regardless of the disk size in the entire range investigated here, and it is strongest around the  $90^\circ$  and  $270^\circ$  directions, because the total scattered intensity into those directions is almost zero.

### 2. Disk lattice

The computed results shown so far correspond to isolated cobalt disks. However, and in order to compare the computed results with those of real experiments,<sup>18</sup> we have implemented a two-dimensional array of disks in our calculation, as shown in Fig. 2. Experimentally, the MO scattering behavior of a single nanodisk cannot be accurately obtained. However, an ordered array, while preserving all the conditions assumed for each individual scatterer, allows for a more efficient measurement of the scattering, not only for the signal increase produced by the large number of objects, but also for its constructive interference effect. The diffracted spots allow for sampling the scattering pattern at different angles simultaneously, while maintaining the very simple normal incidence geometry, where measurements in reflection are not useful because no T-MOKE effect can be expected in such direction.

From the MO response corresponding to single disks, as obtained with the FP calculation, the far-field scattered intensity is computed along the diffraction directions, neglecting any optical interaction between different disks in the array. The lattice equation at normal incidence for horizontal

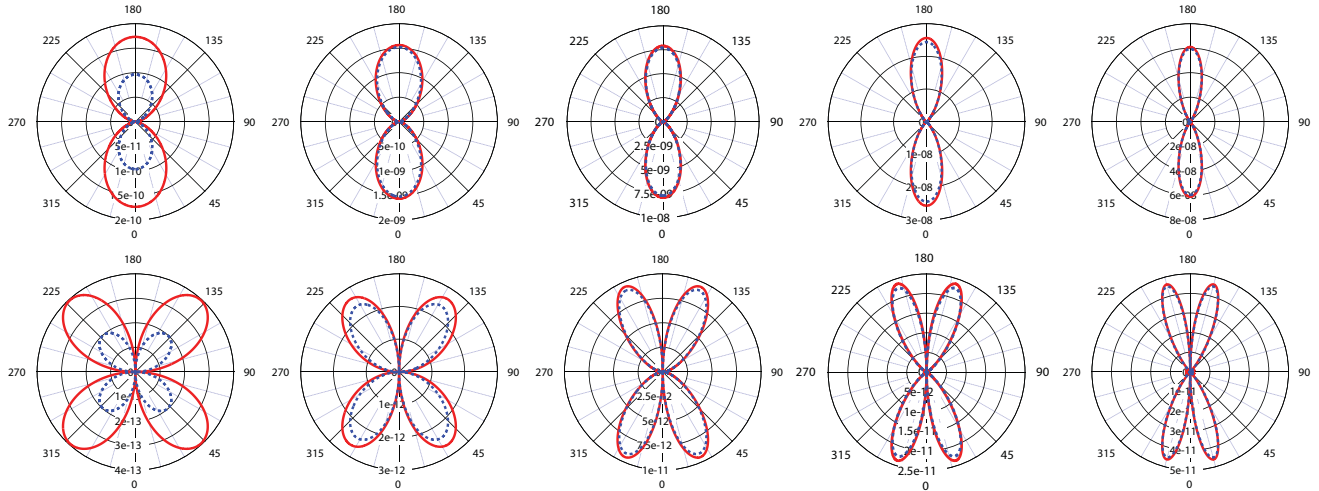


FIG. 5. (Color online) Polar plots of the far-field scattered intensity (first row) and  $\Delta I$  (second row) patterns for several sizes for both the FP and the IL approaches. From left to right, each column corresponds to one disk size, ranging from  $D = 200$  nm to  $D = 400$  nm,  $D = 600$  nm,  $D = 800$  nm, and  $D = 1000$  nm. Solid (red) and dashed (blue) lines correspond to the FP and IL approaches, respectively. The  $\Delta I$  patterns are obtained by computing the difference in scattered intensity under magnetization reversal. Notice that  $0^\circ$  and  $180^\circ$  are the backward and forward directions, respectively, while the incident electric field oscillates in the  $90^\circ$ - $270^\circ$  direction.

observations, i.e., scattering in the  $X$ - $Y$  plane containing both the surface normal and the incident electric field, is

$$m\lambda = a \sin \varphi, \quad (17)$$

where  $m$  is the horizontal diffraction order,  $\lambda$  the incoming light wavelength (*in vacuo*),  $a$  the lattice period, and  $\varphi$  the horizontal diffraction angle, measured with respect to the lattice normal direction. From Eq. (17), one can easily obtain the angular positions at which we must sample the scattered intensity patterns (Fig. 5), given by  $\varphi = \arcsin(\frac{m\lambda}{a})$ .

Figure 6(a) shows the normalized MO signal  $\Delta I/I$  for the case  $D = 200$  nm, as a function of the lattice parameter  $a$  and for several diffraction orders from  $m = 1$  to  $m = 5$ . For each value of  $a$ , the MO signal increases with the order. More precisely, Fig. 6(b) shows that  $\Delta I/I$  vs  $m$  behavior is due to its dependence on the diffraction angle  $\varphi$ . The increase in the T-MOKE signal with the diffraction angle is primarily a direct consequence of the drop in intensity  $I$ , although there is also an increase in the MO signal  $\Delta I$ , simply due to the increase of the diffraction angle  $\varphi$ , as can be seen in Fig. 5, first column second row.

Using this representation, the  $\Delta I/I$  for all the diffracted beams lie on top of each other, with the starting angle depending on the diffraction order. In Fig. 6(b),  $\Delta I/I(\varphi)$  computed using the IL approach is also shown, with an almost perfect match between  $\Delta I/I(\varphi)$  computed using the FP approach. We chose the case  $D = 200$  nm since it presents substantial deviations from the IL approach and therefore allows us to confirm very visibly that the geometric confinement does not substantially affect the far-field results in terms of the magneto-optically induced relative intensity change, which is the conventional experimental observable. The results for all other sizes look nearly identical, i.e., show almost exactly the expected behavior that one would derive from the IL approximation for  $\Delta I/I$ .

The gap between neighboring disks, given as  $g = a - D$ , imposes a minimum for the physically meaningful lattice period corresponding to  $g = 0$ ; i.e.,  $a_{\min} = D$ . However, in order to avoid the near-field optical interactions between the

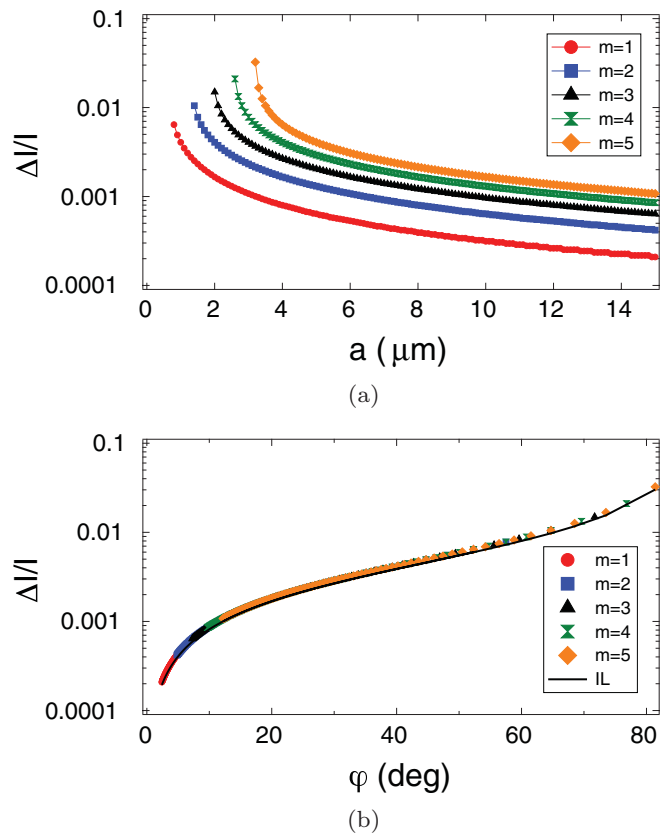


FIG. 6. (Color online) Normalized MO signal for several horizontal diffraction orders  $m$  for  $D = 200$  nm, with  $\lambda = 632.8$  nm. (a)  $\Delta I/I$  vs lattice period. (b)  $\Delta I/I$  vs diffraction angle  $\varphi$ .

disks, which will complicate the issue and is beyond the scope of this work, it is a good experimental strategy to use values that are substantially larger than  $a_{\min}$ , also because this would make more diffraction orders available, i.e., more values of  $\varphi$  accessible, although there should be enough magnetic material in the unit cell in order to keep  $I$  and  $\Delta I$  above the noise level. These considerations are among those to be taken account, when it comes to the design of disk lattices to be used in experiments.

## V. CONCLUSIONS

The main conclusion one can draw from the presented results is the fact that the experimentally accessible  $\Delta I/I$  ratio seems virtually unaffected by the geometric confinement of the disks, despite the remarkable size-induced differences that are found in the dipole moment distributions especially for sub-wavelength disks. We have shown that the insensitivity of the  $\Delta I/I$  ratio to lateral confinement is a consequence of the close similarity of the optical and magneto-optical polarization patterns, irrespective of disk size, and of the fact that their contribution to the far-field intensity scales nearly in the same way.

To discuss this aspect further, we make the following argument of how the magneto-optical response primarily originates.  $E_x$  is the result of the MO effect only because it does not exist in the case without MO coupling. Therefore  $E_x$  is only caused by the  $P_x$  from neighboring dipoles:  $E_x = s_{xx} P_x$  [using the notation of the Appendix; see Eq. (A6)]. Furthermore, the entire dipole  $P_x$  is a small correction being driven by

$E_y$ . Consequently, as a first approximation we can use  $E_y$  from the MO-free system as the leading contribution, or equivalently neglect the MO term,  $\alpha_{\text{off}} E_x$ , for the calculation of  $P_y$ . Thus, we approximate  $P_y \approx P_{y\text{scalar}} = \epsilon_0 \alpha_d E_y$ , where  $P_{y\text{scalar}}$  is the optical component coming from a MO-effect-free, purely scalar calculation without off-diagonal elements in the dielectric tensor, so that

$$P_x \approx P_{x\text{scalar}} = \epsilon_0 \left( \alpha_d s_{xx} P_x + \frac{\alpha_{\text{off}}}{\epsilon_0 \alpha_d} P_{y\text{scalar}} \right), \quad (18)$$

$$P_{x\text{scalar}} = \frac{1}{1 - \epsilon_0 \alpha_d s_{xx}} \frac{\alpha_{\text{off}}}{\alpha_d} P_{y\text{scalar}}. \quad (19)$$

If we now have a look at Eq. (A5) from the Appendix, it can be shown that, neglecting second-order MO terms, i.e.,  $O(\alpha_{\text{off}}^2)$  terms,

$$\frac{1}{1 - \epsilon_0 \alpha_d s_{xx}} = \frac{\alpha_{xx\text{eff}}}{\alpha_d}, \quad (20)$$

so that the approximative relation between the optical and the MO dipole moment components is given as

$$P_{x\text{scalar}} = \frac{\alpha_{xx\text{eff}}}{\alpha_d} \frac{\alpha_{\text{off}}}{\alpha_d} P_{y\text{scalar}}. \quad (21)$$

Figure 7 shows an example of this approximate relation and demonstrates how close this semiscalar approach is to the exact result. Both the primary optical and the MO components for the case  $D = 600$  nm are shown, from both tensorial and scalar calculations, all normalized to the same infinite-layer calculation. This result opens up a pathway to undertake time-efficient calculations of magneto-optical responses, in which

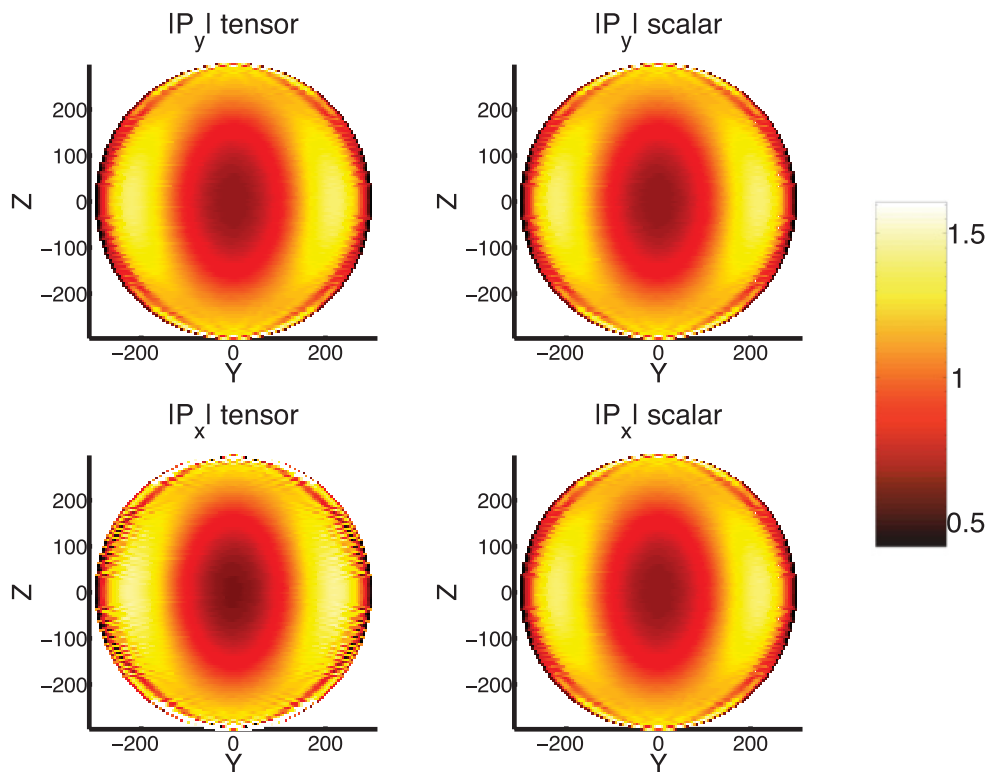


FIG. 7. (Color online) Primary optical (first row) and MO (second row) components for the case  $D = 600$  nm, from both tensorial (left column) and scalar (right column) calculations, all normalized to the IL calculation. The color scale is the same for all the plots.

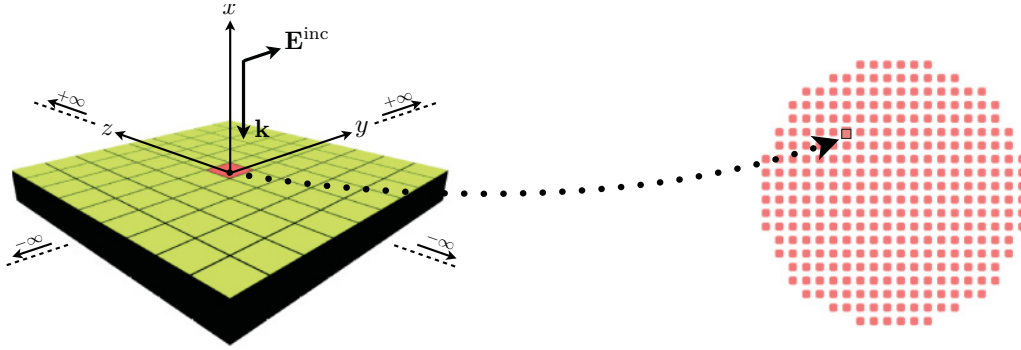


FIG. 8. (Color online) Infinite-layer approach. Every dipole interacts with all the other dipoles. Subsequently, this dipole is inserted in each cell of the discretization mesh to model any arbitrary planar shape (no further interaction is considered).

the true magneto-optical nature of materials is considered only after the confinement-induced optical polarization pattern has been calculated by means of relations similar to Eq. (21). It is, however, important to stress that the scalar approach reached in Eq. (21) no longer holds in conditions of strong MO effect.

As a summary, in this work we have investigated the optical and magneto-optical responses of nanoscale ferromagnetic disks by means of numerical simulations, using a discrete dipole approximation. The disks were illuminated under normal incidence with a wavelength of  $\lambda = 632.8$  nm, assuming the transverse magneto-optical Kerr effect (T-MOKE) configuration. Results show that the strong similarity between the optical and magneto-optical nanoscale confinement effects also results in the fact that the magneto-optically induced far-field light intensity relative change  $\Delta I/I$ , which is the quantity measured in experiments, is only weakly affected even in the case of sub-wavelength-sized disks, so that the far-field predictions coming from a film electromagnetic solution<sup>18</sup> remain highly accurate. We demonstrate this by calculating the diffracted light intensities and intensity changes produced by nanodisk arrays, which are commonly used in experimental studies of nanostructure magneto-optics.

#### ACKNOWLEDGMENTS

This research has been supported by MICINN under project No. FIS2010-21984. Work at nanoGUNE acknowledges funding from the Basque Government under Program No. PI2009-17 and the Spanish Ministry of Science and Education under Project No. MAT2009-07980. R. Alcaraz de la Osa also thanks the Ministry of Education of Spain for his FPU grant. The authors thank F. González for his valuable comments and helpful discussions.

#### APPENDIX: INFINITE-LAYER APPROACH

In the IL approach, the dipole-dipole interactions are assumed to be the same as for an infinite film at every point of the structure, so that any particle can be represented by placing noninteracting dipoles on a properly shaped grid, whose polarizability tensor has been renormalized to include the infinite-film interactions exactly. In the derivation of this approach, each electric dipole interacts with an infinite number

of surrounding electric dipoles, each of which having an electric polarizability  $\bar{\alpha}_j$  given by Eq. (6), as shown in Fig. 8.

The dipole moment acquired by each of these electric dipoles is given by

$$\mathbf{P}_j = \varepsilon_0 \bar{\alpha}_j \left( \mathbf{E}_j^{\text{inc}} + \sum_{k \neq j} \bar{\bar{\mathbf{A}}}_{jk} \mathbf{P}_k \right). \quad (\text{A1})$$

To express this dipole moment in terms of an effective electric polarizability that incorporates all interactions, we define

$$\mathbf{P}_j = \varepsilon_0 \bar{\alpha}_{\text{eff}} \mathbf{E}_j^{\text{inc}}. \quad (\text{A2})$$

For normal incidence radiation, the exciting field as well as the lateral film structure are translationally invariant, so that, assuming all the dipoles have the same electric polarizability tensor  $\bar{\alpha}_j \equiv \bar{\alpha}$ , the resulting polarization pattern also has translational invariance and all electric dipoles within the film acquire the same dipole moment; i.e.,  $\mathbf{P}_j = \mathbf{P}_k = \mathbf{P}_{\text{IL}}$ . Then,

$$\left( \bar{\mathbf{I}} - \varepsilon_0 \bar{\alpha} \sum_{k \neq j} \bar{\bar{\mathbf{A}}}_{jk} \right) \mathbf{P}_{\text{IL}} = \varepsilon_0 \bar{\alpha} \mathbf{E}^{\text{inc}}, \quad (\text{A3})$$

$$\mathbf{P}_{\text{IL}} = \varepsilon_0 \underbrace{\left( \bar{\mathbf{I}} - \varepsilon_0 \bar{\alpha} \sum_{k \neq j} \bar{\bar{\mathbf{A}}}_{jk} \right)^{-1}}_{\bar{\alpha}_{\text{eff}}} \bar{\alpha} \mathbf{E}^{\text{inc}}, \quad (\text{A4})$$

leading to

$$\bar{\alpha}_{\text{eff}} = \left( \bar{\mathbf{I}} - \varepsilon_0 \bar{\alpha} \sum_{k \neq j} \bar{\bar{\mathbf{A}}}_{jk} \right)^{-1} \bar{\alpha}. \quad (\text{A5})$$

For the calculation of the infinite sum in Eq. (A5), a suitable truncation criterion must be established by studying its convergence. For this purpose, we analyzed the “order”  $\frac{1}{2} N^{\frac{1}{2}}$  ( $N$  being the total number of dipoles) dependence of the numerical values. Here we found that calculation of up to an order of 1000, corresponding to 4 000 000 dipoles, allowed for a very accurate extraction of the effective polarizability tensor.

Once converged, the transfer function tensor sum  $\sum_{k \neq j} \bar{\bar{A}}_{jk}$  becomes

$$\sum_{k \neq j} \bar{\bar{A}}_{jk} = \begin{pmatrix} s_{xx} & 0 & 0 \\ 0 & s_{yy} & 0 \\ 0 & 0 & s_{zz} \end{pmatrix}, \quad (\text{A6})$$

with

$$\begin{aligned} s_{xx} &= -6.50 \pm 0.04 \times 10^{35} + i 0 \pm 4 \times 10^{33} [\text{F}^{-1} \text{m}^{-2}], \\ s_{yy} &= 3.24 \pm 0.02 \times 10^{35} + i 2.2 \pm 0.2 \times 10^{34} [\text{F}^{-1} \text{m}^{-2}], \\ s_{zz} &= s_{yy}. \end{aligned}$$

\*alcarazr@unican.es

- <sup>1</sup>L. Novotny and N. van Hulst, *Nature Photonics* **5**, 83 (2011).
- <sup>2</sup>M. I. Stockman, *Phys. Today* **64**(2), 39 (2011).
- <sup>3</sup>V. Giannini, A. I. Fernández-Domínguez, S. C. Heck, and S. A. Maier, *Chem. Rev.* **111**, 3888 (2011).
- <sup>4</sup>J. N. Anker, W. P. Hall, O. Lyandres, N. C. Shah, J. Zhao, and R. P. van Duyne, *Nature Mater.* **7**, 442 (2008).
- <sup>5</sup>K. C. Weng, C. O. Noble, B. Papahadjopoulos-Sternberg, F. F. Chen, D. C. Drummond, D. B. Kirpotin, D. Wang, Y. K. Hom, B. Hann, and J. W. Park, *Nano Lett.* **8**, 2851 (2008).
- <sup>6</sup>R. Quidant and M. Kreuzer, *Nature Nanotechnology* **5**, 762 (2010).
- <sup>7</sup>M. Sandtke and L. Kuipers, *Nature Photonics* **1**, 573 (2007).
- <sup>8</sup>B. C. Stipe, T. C. Strand, C. C. Poon, H. Balamane, T. D. Boone, J. A. Katine, J. Li, V. Rawat, H. Nemoto, A. Hirotsune, O. Hellwig, R. Ruiz, E. Dobisz, D. S. Kercher, N. Robertson, T. R. Albrecht, and B. D. Terris, *Nature Photonics* **4**, 484 (2010).
- <sup>9</sup>P. N. Prasad, *Nanophotonics* (John Wiley Sons, Inc., Hoboken, New Jersey, 2004).
- <sup>10</sup>J. Steele, N. Grady, P. Nordlander, and N. Halas, in *Surface Plasmon Nanophotonics*, Springer Series in Optical Sciences, Vol. 131, edited by M. Brongersma and P. Kik (Springer, Berlin, 2007) pp. 183–196.
- <sup>11</sup>M. Pelton, J. Aizpurua, and G. Bryant, *Laser Photonics Rev.* **2**, 136 (2008).
- <sup>12</sup>N. Insin, J. B. Tracy, H. Lee, J. P. Zimmer, R. M. Westervelt, and M. G. Bawendi, *ACS Nano* **2**, 197 (2008).
- <sup>13</sup>M. Schnell, A. Garcia-Etxarri, A. J. Huber, K. B. Crozier, A. Borisov, J. Aizpurua, and R. Hillenbrand, *J. Phys. Chem. C* **114**, 7341 (2010).
- <sup>14</sup>V. E. Ferry, L. A. Sweatlock, D. Pacifici, and H. A. Atwater, *Nano Lett.* **8**, 4391 (2008).
- <sup>15</sup>V. Myroshnychenko, J. Rodríguez-Fernández, I. Pastoriza-Santos, A. M. Funston, C. Novo, P. Mulvaney, L. M. Liz-Marzan, and F. J. García de Abajo, *Chem. Soc. Rev.* **37**, 1792 (2008).
- <sup>16</sup>R. T. Hill, J. J. Mock, Y. Urzhumov, D. S. Sebba, S. J. Oldenburg, S.-Y. Chen, A. A. Lazarides, A. Chilkoti, and D. R. Smith, *Nano Lett.* **10**, 4150 (2010).
- <sup>17</sup>P. Albella, B. Garcia-Cueto, F. González, F. Moreno, P. C. Wu, T.-H. Kim, A. Brown, Y. Yang, H. O. Everitt, and G. Videen, *Nano Lett.* **11**, 3531 (2011).
- <sup>18</sup>M. Grimsditch and P. Vavassori, *J. Phys. Condens. Matter* **16**, R275 (2004).
- <sup>19</sup>J. B. González-Díaz, A. García-Martín, J. M. García-Martín, A. Cebollada, G. Armelles, B. Sepúlveda, Y. Alaverdyan, and M. Käll, *Small* **4**, 202 (2008).
- <sup>20</sup>P. K. Jain, Y. Xiao, R. Walsworth, and A. E. Cohen, *Nano Lett.* **9**, 1644 (2009).
- <sup>21</sup>J. B. González-Díaz, J. M. García-Martín, A. García-Martín, D. Navas, A. Asenjo, M. Vázquez, M. Hernández-Vélez, and G. Armelles, *Appl. Phys. Lett.* **94**, 263101 (2009).
- <sup>22</sup>V. V. Temnov, G. Armelles, U. Woggon, D. Guzatov, A. Cebollada, A. Garcia-Martin, J. Garcia-Martin, T. Thomay, A. Leitenstorfer, and R. Bratschitsch, *Nature Photonics* **4**, 107 (2010).
- <sup>23</sup>V. I. Belotelov, I. A. Akimov, M. Pohl, V. A. Kotov, S. Kasture, A. S. Vengurlekar, A. V. Gopal, D. R. Yakovlev, A. K. Zvezdin, and M. Bayer, *Nature Nanotechnology* **6**, 370 (2011).
- <sup>24</sup>V. Bonanni, S. Bonetti, T. Pakizeh, Z. Pirzadeh, J. Chen, J. Nogués, P. Vavassori, R. Hillenbrand, J. Åkerman, and A. Dmitriev, *Nano Lett.* **11**, 5333 (2011).
- <sup>25</sup>J. González-Díaz, A. García-Martín, G. Armelles, D. Navas, M. Vázquez, K. Nielsch, R. Wehrspohn, and U. Gösele, *Adv. Mater.* **19**, 2643 (2007).
- <sup>26</sup>J. B. González-Díaz, B. Sepúlveda, A. García-Martín, and G. Armelles, *Appl. Phys. Lett.* **97**, 043114 (2010).
- <sup>27</sup>G. X. Du, T. Mori, S. Saito, and M. Takahashi, *Phys. Rev. B* **82**, 161403 (2010).
- <sup>28</sup>L. Wang, C. Clavero, Z. Huba, K. J. Carroll, E. E. Carpenter, D. Gu, and R. A. Lukaszew, *Nano Lett.* **11**, 1237 (2011).
- <sup>29</sup>J. Chen, P. Albella, Z. Pirzadeh, P. Alonso-González, F. Huth, S. Bonetti, V. Bonanni, J. Åkerman, J. Nogués, P. Vavassori, A. Dmitriev, J. Aizpurua, and R. Hillenbrand, *Small* **7**, 2341 (2011).
- <sup>30</sup>D. A. Smith and K. L. Stokes, *Opt. Express* **14**, 5746 (2006).
- <sup>31</sup>S. Albaladejo, R. Gómez-Medina, L. S. Froufe-Pérez, H. Marínchío, R. Carminati, J. F. Torrado, G. Armelles, A. García-Martín, and J. J. Sáenz, *Opt. Express* **18**, 3556 (2010).
- <sup>32</sup>R. A. de la Osa, P. Albella, J. M. Saiz, F. González, and F. Moreno, *Opt. Express* **18**, 23865 (2010).
- <sup>33</sup>G. C. Tistis, E. Papaioannou, P. Patoka, J. Gutek, P. Fumagalli, and M. Giersig, *Nano Lett.* **9**, 1 (2009).
- <sup>34</sup>B. T. Draine and P. J. Flatau, *J. Opt. Soc. Am. A* **11**, 1491 (1994).
- <sup>35</sup>M. Yurkin, V. Maltsev, and A. Hoekstra, *J. Quant. Spectrosc. Radiat. Transfer* **106**, 546 (2007).
- <sup>36</sup>In the E-DDA, both the electric and magnetic responses of the material are taken into account by considering the excitation of both an oscillating electric and magnetic dipole. In addition, both the relative electric permittivity  $\bar{\bar{\epsilon}}_r$  and the relative magnetic permeability  $\bar{\bar{\mu}}_r$  of the material are second-order (or rank) tensors, although in order to treat magnetic materials in the optical range, we can consider  $\bar{\bar{\mu}}_r = \bar{\bar{1}}$ .
- <sup>37</sup>M. Freiser, *IEEE Trans. Magn.* **4**, 152 (1968).
- <sup>38</sup>E. Purcell, *Electricity and Magnetism*, Berkeley Physics Course, 1st ed., Vol. 1 (McGraw-Hill, New York, 1965).
- <sup>39</sup>J. Jackson, *Classical Electrodynamics*, 2nd ed. (Wiley, New York, 1975).
- <sup>40</sup>C. Kittel, *Introduction to Solid State Physics*, 4th ed. (Wiley, New York, 1986).
- <sup>41</sup>B. T. Draine, *Astrophys. J.* **333**, 848 (1988).
- <sup>42</sup>A. Berger and M. R. Pufall, *J. Appl. Phys.* **85**, 4583 (1999).

<sup>43</sup>For absorbing materials such as metals, the original criterion might not be sufficient, as the skin depth is far smaller than the wavelength.

<sup>44</sup>M. Botchev [<http://www.math.uu.nl/people/vorst/zbeg2.f90>].

<sup>45</sup>B. T. Draine and P. J. Flatau, e-print [arXiv:1002.1505v1](https://arxiv.org/abs/1002.1505v1) (2010).

<sup>46</sup>C. Bohren and D. Huffman, *Absorption and Scattering of Light by Small Particles* (Wiley, New York, 1983).

<sup>47</sup>D. Meneses-Rodríguez, E. Ferreiro-Vila, P. Prieto, J. Anguita, M. U. González, J. M. García-Martín, A. Cebollada, A. García-Martín, and G. Armelles, *Small* **7**, 3317 (2011).

<sup>48</sup>K. Postava, H. Jaffres, A. Schuhl, F. N. V. Dau, M. Goiran, and A. R. Fert, *J. Magn. Magn. Mater.* **172**, 199 (1997).